minerals

MDPI

Article

The Effect of a Hydrogen Reduction Procedure on the Microbial Synthesis of a Nano-Pd Electrocatalyst for an Oxygen-Reduction Reaction

Jingwen Huang [1,†], Guoqing Zhang [1,†], Xiaoting Deng [2], Qingxin Li [1], Haikun Zhou [3], Zhiyong Xie [2], Xueduan Liu [1], Feng Liu [4,*] and Yili Liang [1,*]

[1] School of Minerals Processing and Bioengineering, Central South University, Changsha 410083, China; huangjingwen@csu.edu.cn (J.H.); 195611018@csu.edu.cn (G.Z.); lizzy-37@163.com (Q.L.); xueduanliu@csu.edu.cn (X.L.)
[2] State Key Laboratory of Powder Metallurgy & Science and Technology on High Strength Structural Materials Laboratory, Central South University, Changsha 410083, China; xiaotingdeng@126.com (X.D.); xzy507@csu.edu.cn (Z.X.)
[3] School of Chemical Engineering, University of New South Wales, Sydney, NSW 2052, Australia; hector.zhou@unsw.edu.au
[4] State Key Laboratory of Advanced Technologies for Comprehensive Utilization of Platinum Metals, Kunming Institute of Precious Metals, Kunming 650106, China
* Correspondence: feng.liu@spmcatalyst.com (F.L.); liangyili6@csu.edu.cn (Y.L.)
† These authors contributed equally to this work.

check for updates

Citation: Huang, J.; Zhang, G.; Deng, X.; Li, Q.; Zhou, H.; Xie, Z.; Liu, X.; Liu, F.; Liang, Y. The Effect of a Hydrogen Reduction Procedure on the Microbial Synthesis of a Nano-Pd Electrocatalyst for an Oxygen-Reduction Reaction. *Minerals* **2022**, *12*, 531. https://doi.org/10.3390/min12050531

Academic Editors: Carolina Cruz Viggi, Federico Aulenta, Abraham Esteve-Núñez and Naoko Okibe

Received: 18 March 2022
Accepted: 22 April 2022
Published: 24 April 2022

Abstract: Noble-metal electrocatalysts supported by biological-organism-derived carbons have attracted attention from the public due to the growing demands for green synthesis and environmental protection. Carbonization at high temperatures and hydrogen reduction are critical steps in this technical route. Herein, *Shewanella oneidensis* MR-1 were used as precursors, and the effects of the hydrogen-reduction procedure on catalysts were explored. The results showed that the performances of FHTG (carbonization followed by hydrogen reduction) displayed the best performance. Its ECSA (electrochemical surface area), MA (mass activity), and SA (specific activity) reached 35.01 $m^2\ g^{-1}$, 58.39 $A{\cdot}g^{-1}$, and 1.66 $A\ cm^{-2}$, respectively, which were 1.17, 1.75, and 1.50 times that of PHTG (prepared through hydrogen reduction followed by carbonization) and 1.56, 2.26, and 1.44 times that of DHTG (double hydrogen reduction). The high performance could be attributed to its fine particle size and rich N content, and the specific regulation mechanism was also proposed in this paper. This study opens a practical guide for effectively avoiding particle agglomeration during the fabrication process for catalysts.

Keywords: Bio-PdNPs; hydrogen reduction; oxygen-reduction reaction

1. Introduction

Increasing demand for clean and sustainable energy triggered the exploration of proton-exchange membrane fuel cells (PEMFC) [1,2]. However, the cathodic oxygen-reduction reaction (ORR) of PEMFC is sluggish, which requires electrocatalysts to maintain efficient operation [3,4]. Therefore, it is of great significance to develop catalysts with low cost, high activity, and good stability. Palladium (Pd) is a member of the platinum (Pt) group of elements, and palladium nanoparticles (PdNPs) have been extensively investigated and applied in various processes [5]. The conventional synthesis of metal-NPs (with the utilization of organic solutions and complicated physiochemical methods) is far from the concept of green chemistry [6,7], and there is still room for the development of greener concepts.

As a "preparation factory" for nanoparticles, micro-organisms have many advantages, such as wide variety, rapid reproduction, controllable synthesis, large-scale production, and environmental friendliness [8,9]. Using micro-organisms as precursors can provide flexible modulation of particle size and surface morphology. Many bacteria (such as *Desulfovibrio desulfuricans* [10], *Shewanella oneidensis* [11,12], *Escherichia coli* [13], and *Geobacter sulfurreducens* [14]) have been reported as catalyst supports, whose mechanisms and influential factors have been widely discussed [15]. It was widely accepted that micro-organisms adsorb metals at a low pH and perform direct and autocatalytic reduction [16,17]. Additionally, current optimizations mainly focus on the effects of electron donors, palladium concentration, pH, temperature, etc. [18,19].

However, Bio-PdNPs are rarely used as commercial electrocatalysts because of their low loading amount and poor electrical conductivity and stability [3,20]. In particular, low conductivity would hinder the electron transfer between electrodes and PdNPs [21]. In order to resolve these problems, methodologies such as doping heteroatoms [22,23], constructing composite conductive carriers [24], and high-temperature carbonization [25,26] have been proposed. High-temperature carbonization is a common method to improve cell conductivity, but aggregation is inevitable in this process, causing sacrificed performances, low yield, excessive energy consumption, and increased fabrication cost [25]. Therefore, how to diminish aggregation while obtaining a good electrical conductivity is the main consideration during the Research & Development of catalyst synthesis.

Shewanella oneidensis MR-1 (MR-1) is a typical dissimilatory metal-reducing bacteria whose abundant functional groups and high N content make it an excellent carrier for noble metal catalysts [27,28]. PdNPs supported on *Shewanella* exhibit excellent electrocatalytic activity for ORR in an alkaline or acid medium [12,29]. Since the *Shewanella*-supported Pd catalyst is prepared through the adsorption of Pd-containing salt followed by subsequent hydrogen reduction and carbonization, it is supposed that the reductive and thermal history has a close relationship with the size/distribution of PdNPs and surface morphology of the carbon support. Herein, the effect of the hydrogen-reduction procedure on the structure and performance of the catalyst is investigated. Three treatments processes were set up, including hydrogen reduction before carbonization, hydrogen reduction after carbonization, and hydrogen reduction before and after carbonization, respectively. The results showed that carbonization followed by hydrogen reduction had obvious advantages, mainly ascribed to Pd particle refinement, uniform dispersion, high integrity, and N-doping. This work broadened the understanding of the interactions between biological Pd/C catalysts and the hydrogen-reduction preparation process and provided a better design idea for the synthesis of electrocatalysts by environmentally versatile bacteria.

2. Materials and Methods

2.1. Bacterial Strain and Growth Condition

The target strain was *Shewanella oneidensis* MR-1 (MR-1), which was purchased from American Type Culture Collection. It was grown in Luria–Bertani medium under conditions of 30 °C and 170 rpm. After activation, the strain was inoculated and expanded to 900 mL with a final OD_{600} = 1.1.

2.2. Biosorption of Palladium

The cultured bacteria were collected by centrifuging at 9000 rpm for 8 min and washed once with phosphate buffer and distilled water, respectively. Then, the cells were resuspended in 100 mL sterile water (pH = 3), followed by dropwise addition of 300 mL 6.89 mM/L Na_2PdCl_4 solution (pH = 3.0) under continuous stirring. All pHs were adjusted by HCl. Ultimately, the samples were centrifuged again and freeze-dried in vacuum.

2.3. Synthesis of Electrocatalysts

The synthesis of electrocatalysts was completed in tubular furnace after cell biosorption, following: (1) air pre-oxidation, (2) hydrogen reduction, and (3) high-temperature carbonization. In this study, three treatments were set up by controlling the sequence of the reduction and carbonization stages: previous-hydrogen treated group (PHTG), final-hydrogen treated group (FHTG), and double-hydrogen treated group (DHTG), respectively.

Previous-hydrogen treated group (PHTG):

The sample was activated in the tube furnace at 200 °C for 2 h under air flow (3 °C min^{-1}), then Pd^{2+} was reduced at 200 °C for 2 h under Ar/H_2 flow (flow ratio 3:1). Ultimately, it was carbonized at 800 °C for 3 h under Ar flow.

Final-hydrogen treated group (FHTG):

The sample was activated in the tube furnace at 200 °C for 2 h under air flow (3 °C min^{-1}), then carbonized at 800 °C for 3 h under Ar flow. Ultimately, Pd^{2+} was reduced at 200 °C for 2 h under Ar/H_2 flow (flow ratio 3:1).

Double-hydrogen treated group (DHTG):

The sample was treated the same as PHTG, and then Pd^{2+} was reduced at 200 °C for 2 h under Ar/H_2 flow (3 °C min^{-1}) again.

2.4. Morphology and Microstructure Characterization

Transmission electron microscopy (TEM, JEM-2100F, JEOL, Tokyo, Japan) was used to characterize structure and particle size. Raman spectrum (using Renishaw inVia spectrometer; Renishaw, Gloucestershire, UK) and X-ray diffraction (XRD, using Bruker Advance D8 X-ray diffractometer; Bruker, Billerica, MA, USA) were performed to analyze the integrity and crystal structure of electrocatalysts, respectively. The chemical states and element content were analyzed by X-ray photoelectron spectroscopy (XPS, ESCALAB250X; Thermo Fisher Scientific, Waltham, MA, USA). The content of Pd was obtained by the inductively coupled plasma (ICP 7000 SERIES; Thermo Fisher Scientific, Waltham, MA, USA).

2.5. Electrochemical Characterization

The electrochemical tests were conducted in 0.1 M oxygen-saturated KOH solution at 25 °C. Glassy carbon electrode (0.196 cm^{-2}), Pt sheet electrode (1 cm × 1 cm, Pt > 99.99%), and Ag/AgCl electrode were installed as working electrode, counter electrode, and reference electrode, respectively. The catalyst ink was prepared by mixing 4 mg sample in 760 μL water, 200 μL ethanol, and 40 μL nafion (5 wt%), which was sonicated for 30 min to form homogeneous ink. The ink (15 μL) was dropped onto the working electrode and dried at 25 °C. Cyclic voltammetry (CV) test was performed in the potential from −1 to 0.3 V at a scan rate of 10 mV s^{-1}. Linear sweep voltammetry (LSV) test was performed in the potential from −0.8 to 0.4 V at a scan rate of 10 mV s^{-1}. Accelerated degradation testing (ADT) was performed under potential from −1 V to 0.3 V and scan rate of 50 mV s^{-1} after 2000 cycles.

3. Results

3.1. Characterization of Morphology and Microstructure

XRD analysis was performed for three Pd/*Shewanella* specimens, and the result is shown in Figure 1. Obvious diffraction peaks at $2\theta = 40.1°$, $2\theta = 46.65°$, and $2\theta = 68.1°$ could be observed in all samples, corresponding to Pd (111), Pd (200), and Pd (220) planes, respectively. The results showed that PdNPs had a face-centered cubic (FCC) structure [30], indicating the successful deposition of well-crystallized Pd particles on micro-organisms.

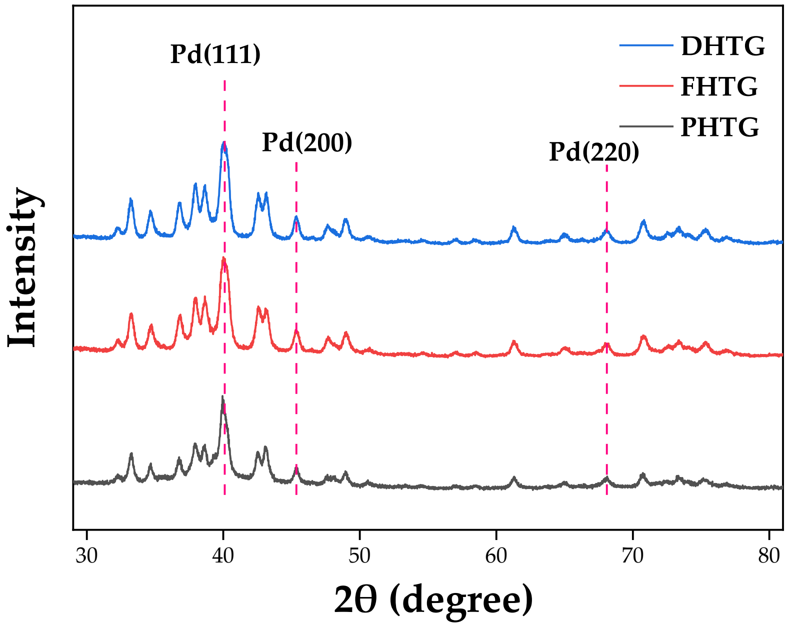

Figure 1. X-ray diffraction patterns of three Pd/*Shewanella* electrocatalysts.

TEM images are shown in Figure 2. PdNPs attached to bacteria were clearly observed without significant agglomeration. This was because bacteria could secrete active substances to provide a large number of binding sites [31]. As a result, well-dispersed nanoparticles could be easily deposited on the surface of the micro-organism support with strong interaction between their interface, which was conducive to improved activity and stability [32,33]. In addition, a further careful observation revealed that both the morphology of bacteria and the particle size of PdNPs were quite different among all samples. The bacteria support of DHTG lost its original structure, while the other two groups kept their morphology well. Most notably, the morphology of FHTG was the most well-preserved, where the uniform distribution of PdNPs could be noticed with an average particle size of 8.55 nm. By contrast, PHTG had an average particle size of 17.71 nm, similar to that of DHTG (18.42 nm). On account of the 1–50 nm particle size of bio-catalysts in previous studies, it seems that the strategy in this work was successful and had desirable catalytic performance when it was less than 10 nm [34,35]. Thus, it could be inferred that FHTG was the best among all samples.

The global annual cost of replacement or regeneration due to the inactivation of industrial catalysts caused by thermal or chemically induced particle aggregation is enormous, which reveals the significance of close attention to the fabrication process. Herein, three catalysts with inconsistent sizes and distributions were prepared by different processes, which further inspired us to explain the mechanisms behind the results.

The Ostwald ripening mechanism has been proposed to interpret metal nanoparticle aggregation [36,37], which suggests that larger particles grow with interparticle transport of mobile species at the expense of smaller particles nearby because larger particles are more energetically stable over smaller particles. The migration–coalescence process was also proposed to cause the metal aggregation, which involved the Brownian motion of metal nanoparticles on the catalyst surface, leading to the formation of larger particles when the small particles came in close proximity to each other [38]. Yuan observed that small nanoparticles could directly form large particles through migration and coalescence, and the large particles further aggregated with the small particles nearby via the Ostwald ripening [39]. This confirmed that different mechanisms simultaneously occurred in the nanoparticle aggregation of one sample. PHTG displayed a larger particle size, which was prepared through hydrogen reduction followed by carbonization. It can be speculated that the initial hydrogen reduction produced metal palladium continuously, resulting in migration–coalescence and Ostwald ripening. Double hydrogen reduction in DHTG seemed to further deteriorate the size distribution of PdNPs, which was not helpful for particle refinement and size distribution optimization.

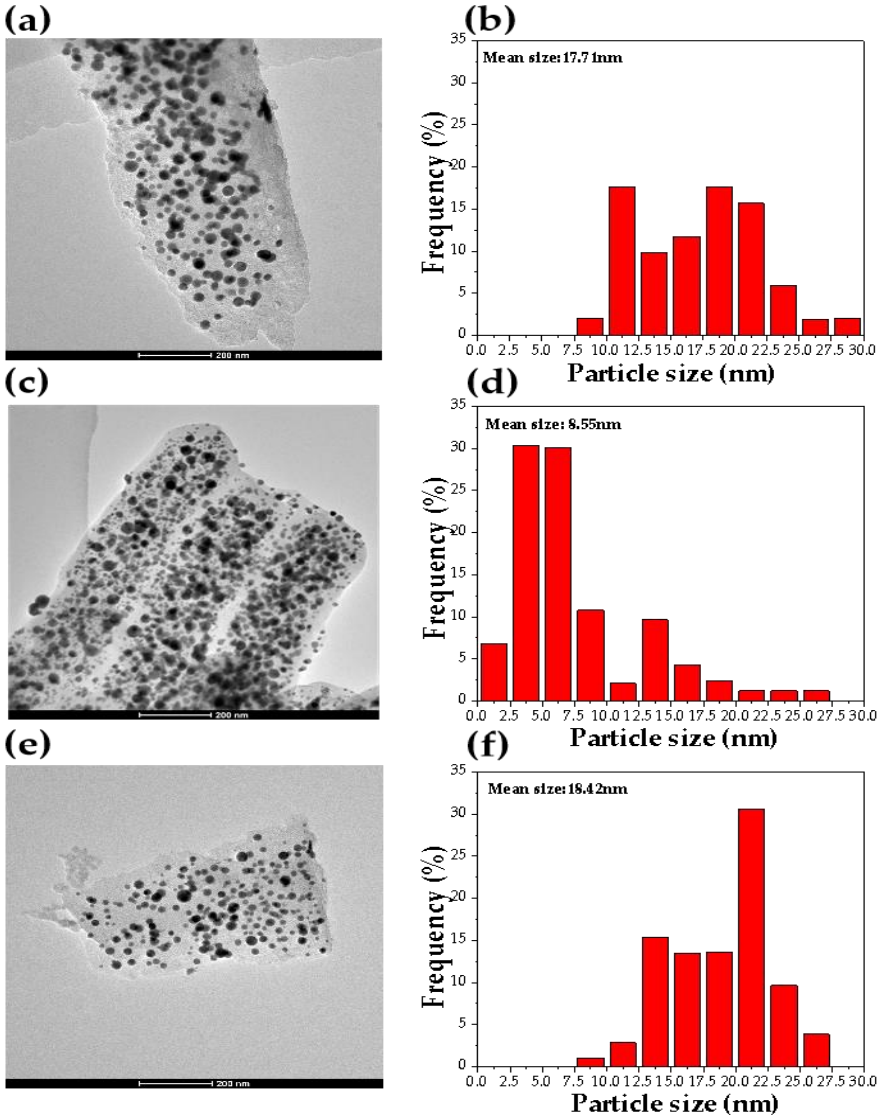

Figure 2. TEM and particle size distribution of PHTG (**a**,**b**), FHTG (**c**,**d**), DHTG (**e**,**f**).

In addition, this demonstrated that carbon was not only the catalyst carrier but also an important factor in controlling particle size and distribution. Carbon layers can be loaded to encapsulate the metal nanoparticles, acting as physical barriers to hinder migration and aggregation [38]. For example, Zhan reported that Au nanoparticles covered with a carbon layer derived from pre-coordinated dopamine carbonization could improve stability and avoid agglomeration [40,41]. In the present work, the PdNPs of FHTG had the smallest size and the best distribution among all samples. It can be speculated that the initial carbonization produced a lot of amorphous carbon and formed a specific structure in which the metal palladium was fixed in a certain space so that the migration–coalescence and Ostwald ripening during hydrogen reduction are effectively inhibited. It could be expected that FHTG tends to exhibit the optimal catalytic performance because, generally, smaller particles tend to yield a larger specific surface area for contact between active substances and reactants.

Figure 3 shows the Raman test results. The D band and G band associated with the defective graphene layers were located at 1346 cm^{-1} and 1580 cm^{-1}, belonging to the first and second-order scattering band, respectively [42]. Distinct peaks indicated the electronic effects of nitrogen and oxygen incorporation on carbon structure [43], which was consistent with the previous discussion that bacteria had abundant functional groups benefiting the performance of catalysts. The ID/IG values were 1.42, 1.29, and 1.52 for PHTG, FHTG, and DHTG, respectively. A lower ID/IG value represents a lower number of defects and better integrity [42]. Therefore, the disorder degree of these samples is as follows: DHTG > PHTG > FHTG, which was in accordance with the TEM observation.

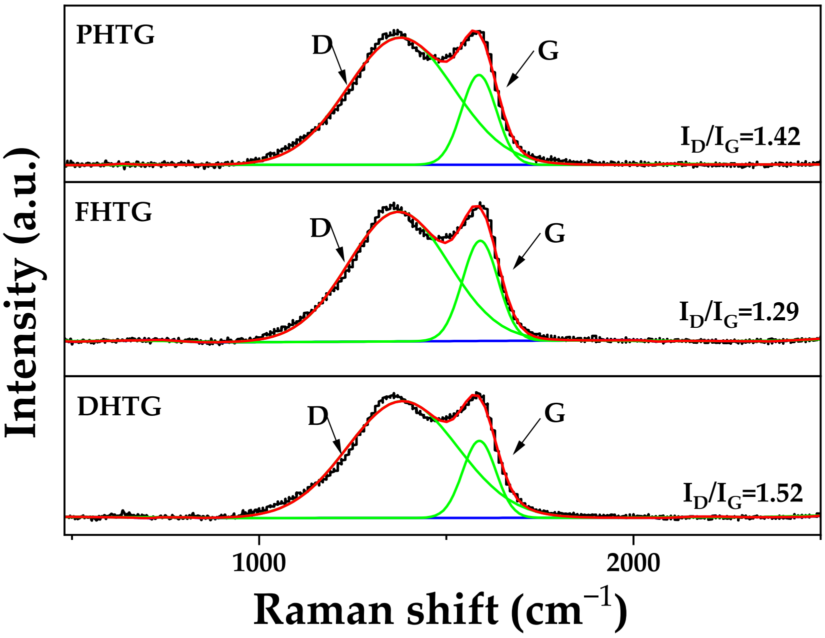

Figure 3. Raman spectra of three Pd/*Shewanella* electrocatalysts.

3.2. Characterization of Elements and Valence States

XPS is an important method to characterize the composition and valence of elements in nanomaterials; the result is shown in Figure 4. The total content of C in the three samples showed little difference, and the O content exceeded 10%, which is beneficial for the tight binding between Pd and carriers. Contents of Pd and N are closely related to the performance and stability of the catalysts. As can be seen from Table 1, the contents of Pd and N in FHTG reached 5.38 wt% and 1.26 wt%, respectively, higher than that in PHTG.

In order to better compare the catalysts and understand the catalytic mechanism, high-resolution XPS spectra of Pd3d were further analyzed. Two peaks at 337.4 eV and 342.7 eV corresponded to Pd^0, and the other doublets at 335.9 eV and 341.2 eV were associated with Pd^{2+} [44], and Pd^0 dominates in all samples. The distributions of Pd in PHTG and FHTG were quite similar, where the former sample displayed 67.91% Pd^0 and 32.09% Pd^{2+}, while the latter one possesses 63.09% Pd^0 and 36.91% Pd^{2+}. Notably, the content of Pd^0 in DHTG (83.83%) was significantly higher than that in the other two groups (Table 2). This result further verified that additional hydrogen reduction produced more Pd(0) from PdO, which leads to the coalescence of PdNPs.

Additionally, the dispersion and deposition of Pd could be promoted by N. The O–O bond could be weakened by the lone electron pair of N, so the performance of PdNPs could be further enhanced by electron-rich nitrogen. Herein, pyridinic-N, pyrrolic-N, and oxidized-N were analyzed [21]. Previous studies have shown that pyridinic-N plays an important role in catalytic activity and stability [45,46]. FHTG had the highest pyridinic-N (47.01%), while the difference between the other two groups (37.74% and 38.53%) was small. Meanwhile, the content of pyrrolic-N in the three samples was basically the same. Thus, it can be inferred that FHTG tends to exhibit superior ORR catalytic performance over the other samples.

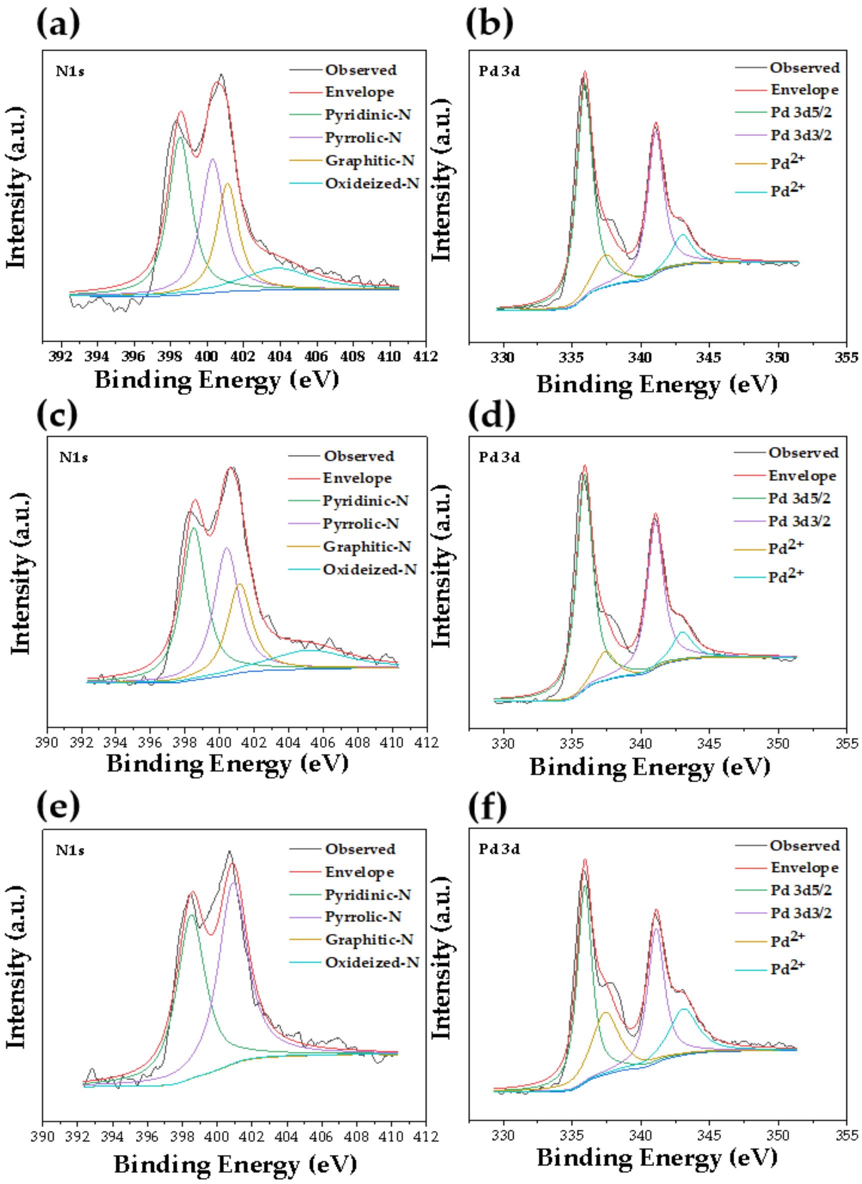

Figure 4. XPS analysis of N 1s and Pd 3d of PHTG (**a**,**b**), FHTG (**c**,**d**), and DHTG (**e**,**f**).

Table 1. Elemental content of PHTG, FHTG, and DHTG.

Samples	C	O	N	Pd
PHTG	80.95	13.12	4.61	1.03
FHTG	80.46	12.9	5.38	1.26
DHTG	81.63	12.13	5.2	1.32

Table 2. Chemical state and content of Pd and N in PHTG, FHTG, and DHTG.

Samples	Pd (%)		N (%)		
	Pd(0)	PdO	Pyridinic-N	Pyrrolic-N	Oxidized-N
PHTG	67.91	32.09	37.43	53.82	8.44
FHTG	63.09	36.91	47.01	52.29	0.7
DHTG	83.83	16.17	38.53	53.01	8.46

Contents of N are closely related to the performance and stability of the catalysts. The increase in N can improve the electron conduction capacity and support surface deficiencies to outperform the electrocatalysis process [44]. In general, the thermochemical process decreases the nitrogen functionalities, and primarily quaternary, pyridinic oxide, pyrrolic-N, and pyridinic-N remain after the thermal process due to their higher persistence [47]. Nitrogen is found to work as an efficient N-functional group alternative in the electrocatalytic process. C-N is one of the most abundant chemical bonds and widely exists in microbiological molecules. The high dissociation energy of the C-N bond makes it highly stable and inert. However, it has been found that the C-N bond is liable to break and undergoes a chemical reaction in the presence of transition metals such as PdNPs, resulting in arylation [48], alkylation [49], alkynylation [50], and cyclization [51] reactions. Therefore, the rupture of the C-N bond under the catalysis of PdNPs can explain the decrease in N content in PHTG and DHTG compared with FHTG. However, the content and type of N are affected by many factors (thermal temperature, thermal method, chemical reagent, pressure, residence time, etc.) [52]. The specific mechanisms need to be further studied.

3.3. ORR Activity of Three Pd/Shewanella Electrocatalysts

Cyclic voltammetry (CV) tests were performed in an O_2-saturated alkaline solution (0.1 M KOH) to assess the catalytic performance of the three electrocatalysts. It can be seen in Figure 5 that obvious oxygen-reduction peaks of PHTG and FHTG were similar and appeared at 0.824 V and 0.820 V (vs. RHE), respectively. Additionally, the ORR peak of DHTG was more negative (0.756 V vs. RHE), probably due to the presence of coalesced PdNPs and poor surface morphology of the catalyst support.

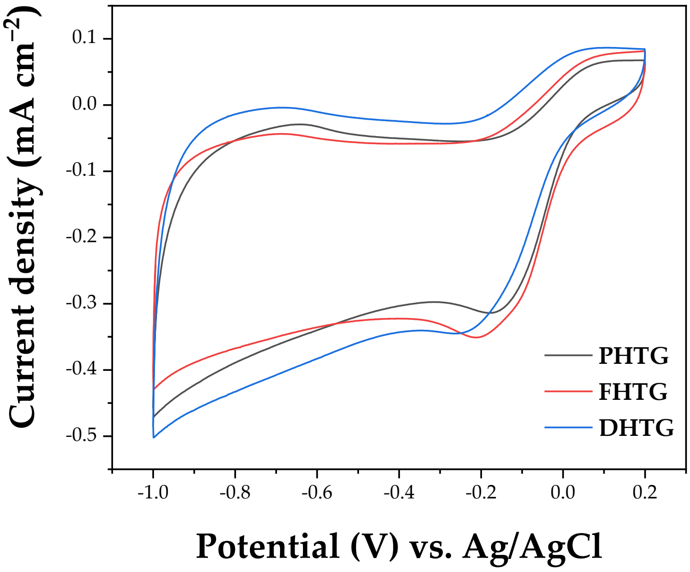

Figure 5. CV curves of PHTG, FHTG, and DHTG in O_2-saturated 0.1 M KOH with a scan rate of 10 mV s^{-1}.

The linear sweep voltammetry was conducted from 400 rpm to 2025 rpm (Figure 6). The diffusion limiting current density of FHTG was the highest (3.377 mA·cm^{-2}), compared with 3.204 mA·cm^{-2} and 3.054 mA·cm^{-2} for PHTG and DHTG, respectively. The half-wave potentials were 0.725 V, 0.732 V, and 0.686 V for PHTG, FHTG, and DHTG, respectively (vs. RHE). According to the following equation, the dynamic current density (j_k), specific activity (SA), mass activity (MA), and electrochemical surface area (ECSA) were calculated [53]:

$$\text{ECSA} = \frac{Q}{424 \times \text{Pd}_{\text{load}}} \quad (1)$$

$$\frac{1}{j} = \frac{1}{j_d} + \frac{1}{j_k} \tag{2}$$

$$MA = \frac{j_k}{Pd_{load}} \tag{3}$$

$$SA = \frac{MA}{ECSA} \tag{4}$$

where Pd_{load} of PHTG, FHTG, and DHTG (measured by ICP) are 11.7%, 12.3%, and 15.1%, respectively. Q is the charge for O_2 reduction from −1.0 V to 0.2 V and j and j_d are the measured current density and limit diffusion current density. As shown in Table 3, FHTG exhibited the highest ECSA, MA, and SA, which were 35.01 $m^2 \cdot g^{-1}$, 58.39 $A \cdot g^{-1}$, and 1.66 $A \cdot m^{-2}$, respectively. The ECSA and MA of DHTG were the lowest among the three groups, decreasing to 22.40 $m^2 \cdot g^{-1}$ and 25.78 $A \cdot g^{-1}$, respectively. In comparison, the MA, SA, and ECSA of FHTG were 1.17, 1.75, and 1.50 times that of PHTG and 1.56, 2.26, and 1.44 times that of DHTG. Although additional hydrogen reduction could yield more Pd(0) through a reduction in PdO, the enlarged PdNPs are not preferable for catalytic activity due to the decreased contact area with reactants, which means one-time hydrogen reduction was optimal. FHTG showed the best performance due to its finest particle size, highest N content, and best integrity among the three samples [54].

Table 3. Electrochemical properties of the three Pd/*Shewanella* electrocatalysts (@−0.1 V vs. Ag/AgCl).

Samples	ECSA ($m^2 \cdot g^{-1}$)	MA ($A \cdot g^{-1}$)	SA ($A \cdot m^{-2}$)	Onset Potential (V)	Half-Wave Potential (V)
PHTG	30.21	33.44	1.11	0.011	−0.242
FHTG	35.01	58.39	1.66	−0.002	−0.235
DHTG	22.40	25.78	1.15	−0.037	−0.281

To further reveal the mechanism of the oxygen-reduction reaction (ORR), LSV measurements were carried out at different rotation rates in a 0.1 M KOH solution. It can be seen in Figure 6 that the diffusion current density increased with the increase in the rotating speed and was proportional to the inverse of its square root. The number of electron transfers per mole of O_2 at −0.25 V, −0.3 V, −0.35 V, −0.4 V, and −0.45 V (vs. Ag/AgCl) was calculated based on the Koutecký–Levich equation [55]. They were 3.95, 3.58, 3.40, 3.26, and 3.17 for PHTG; 3.82, 3.48, 3.32, 3.27, and 3.26 for FHTG; and 2.25, 2.37, 2.39, 2.43, and 2.46 for DHTG, respectively. The results indicated that the ORR of PHTG and FHTG was mainly a four-electron process, while the ORR of DHTG tended to display a two-electron process.

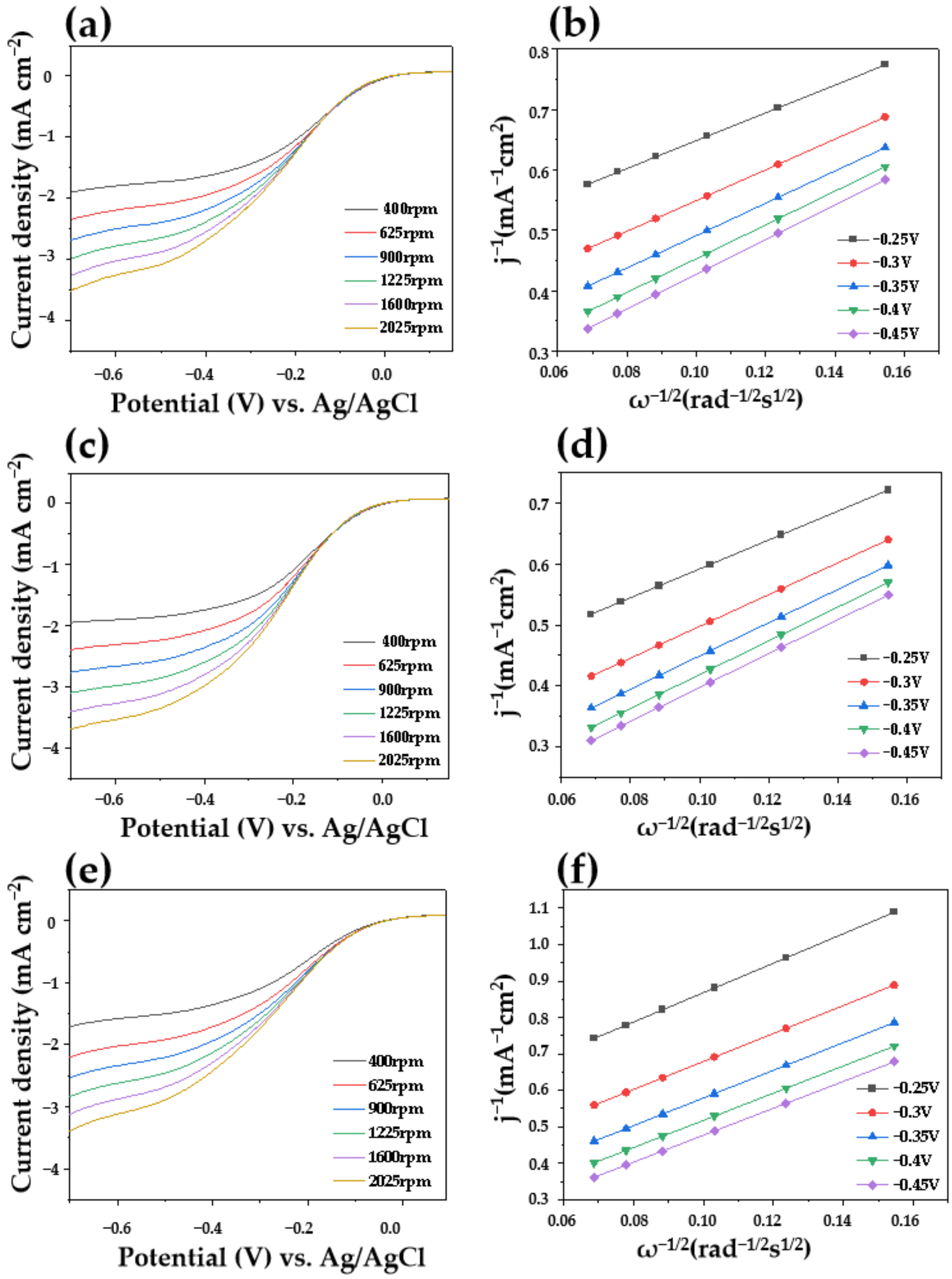

Figure 6. LSV curves (**a**,**c**,**e**) and the Koutecký–Levich plots (**b**,**d**,**f**) at different potentials of PHTG (**a**,**b**), FHTG (**c**,**d**), and DHTG(**e**,**f**).

The stability of the catalyst was closely related to its service life, which affected the cost of PEMFC. To test the stability of the three catalysts, 2000 cycles of accelerated degradation testing (ADT) were performed in an O_2-saturated alkaline solution (0.1 M KOH). After 2000 cycles, the limiting current densities were 2.89 mA·cm^{-2} for PHTG, 3.23 mA·cm^{-2} for FHTG, and 2.92 mA·cm^{-2} for DHTG, which decreased by 9.69%, 4.44%, and 4.26%, respectively. The oxygen-reduction peaks were at 0.8106 V, 0.8136 V, and 0.7426 V (vs. RHE), which decreased by 1.58%, 0.69%, and 3.01%, respectively (Figure 7). It was obvious that FHTG showed outstanding stability compared with the other two groups in this work. The best stability of FHTG could be attributed to its high pyrrolic N, pyridinic N content, and intact support structure [56]. The results confirmed that maintaining the structural integrity of the carrier was also beneficial to improving the activity and corrosion resistance of the catalyst.

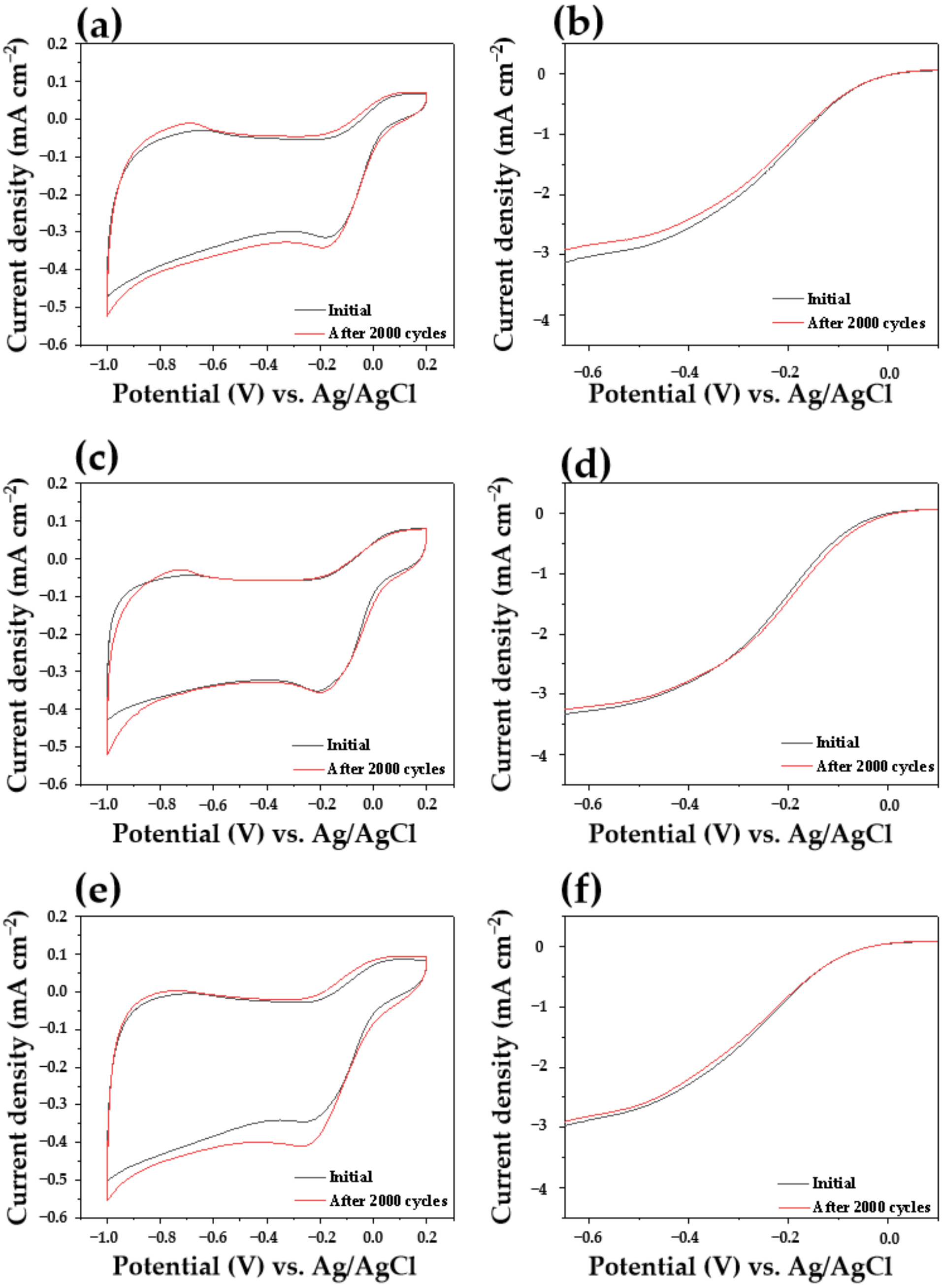

Figure 7. CV curves (**a**,**c**,**e**) and LSV curves (**b**,**d**,**f**) for initial state and after 2000 cycles of PHTG (**a**,**b**), FHTG (**c**,**d**), and DHTG (**e**,**f**).

4. Conclusions

Well-dispersed nanoparticles could be easily deposited on the surface of *Shewanella oneidensis* MR-1, with strong interfacial interaction, and Pd-based electrocatalysts with improved activity and stability could be obtained. The reductive and thermal history has a close relationship with the size/distribution of PdNPs and the surface morphology of the carbon support. Prior carbonization can effectively reduce aggregation, and electrochemical tests showed that FHTG had the best ORR activity and stability under alkaline conditions. The enhanced catalytic performance of FHTG could be attributed to its highest structural integrity and N content, the best uniform distribution of PdNPs, and the finest particle size. Herein, it was proposed that the amorphous carbon layer formed by carbonization can effectively separate PdNPs and prevent Ostwald ripening and the migration–coalescence process. In addition, PdNPs produced by prior reduction can catalyze the rupture of the C-N bond, which leads to a decrease in N content. Moreover, additional hydrogen reduction could yield more Pd(0) through a reduction in PdO, but the enlarged PdNPs were not preferable for catalytic activity due to the decreased contact area with reactants. The bacterium with multiple reductions showed an extremely high degree of disorder, causing structure defect, serious agglomeration, and decreased stability.

Author Contributions: Conceptualization, J.H., Q.L., G.Z., X.D., Z.X., X.L. and Y.L.; methodology, J.H., Q.L., G.Z., F.L. and Y.L.; software, Q.L.; validation, J.H., Q.L. and Y.L.; formal analysis, X.D., Z.X., X.L. and F.L.; writing—original draft preparation, J.H. and Y.L.; writing—review and editing, J.H., G.Z., H.Z. and Y.L.; visualization, J.H., G.Z., Q.L. and Y.L.; funding acquisition, Y.L. and F.L. All authors have read and agreed to the published version of the manuscript.

Funding: This research was funded by the National Key Research and Development Program of China (no.2018YFB1502502) and the fund of the State Key Laboratory of Advanced Technologies for comprehensive Utilization of Platinum Metals (no. SKL-SPM-202003).

Conflicts of Interest: The authors declare no conflict of interest.

References

1. Jiao, K.; Xuan, J.; Du, Q.; Bao, Z.M.; Xie, B.A.; Wang, B.W.; Zhao, Y.; Fan, L.H.; Wang, H.Z.; Hou, Z.J.; et al. Designing the next generation of proton-exchange membrane fuel cells. *Nature* **2021**, *595*, 361–369. [CrossRef]
2. Shi, S.; Wen, X.L.; Sang, Q.Q.; Yin, S.; Wang, K.L.; Zhang, J.; Hu, M.; Yin, H.M.; He, J.; Ding, Y. Ultrathin nanoporous metal electrodes facilitate high proton conduction for low-Pt PEMFCs. *Nano Res.* **2021**, *14*, 2681–2688. [CrossRef]
3. Fan, J.; Chen, M.; Zhao, Z.; Zhang, Z.; Ye, S.; Xu, S.; Wang, H.; Li, H. Bridging the gap between highly active oxygen reduction reaction catalysts and effective catalyst layers for proton exchange membrane fuel cells. *Nat. Energy* **2021**, *6*, 475–486. [CrossRef]
4. Pan, L.; Ott, S.; Dionigi, F.; Strasser, P. Current challenges related to the deployment of shape controlled Pt alloy ORR nanocatalysts into low-Pt loaded cathode layers of Proton Exchange Membrane Fuel Cells (PEMFC). *Curr. Opin. Electrochem.* **2019**, *18*, 61–71. [CrossRef]
5. Chen, Z.; Vorobyeva, E.; Mitchell, S.; Fako, E.; Ortuno, M.A.; Lopez, N.; Collins, S.M.; Midgley, P.A.; Richard, S.; Vile, G.; et al. A heterogeneous single-atom palladium catalyst surpassing homogeneous systems for Suzuki coupling. *Nat. Nanotechnol.* **2018**, *13*, 702–707. [CrossRef] [PubMed]
6. Ali, I.; Peng, C.; Khan, Z.M.; Naz, I.; Sultan, M.; Ali, M.; Abbasi, I.A.; Islam, T.; Ye, T. Overview of microbes based fabricated biogenic nanoparticles for water and wastewater treatment. *J. Environ. Manag.* **2019**, *230*, 128–150. [CrossRef]
7. Vysakh, A.B.; Shebin, K.J.; Jain, R.; Sumanta, P.; Gopinath, C.S.; Vinod, C.P. Surfactant free synthesis of Au@Ni core-shell nanochains in aqueous medium as efficient transfer hydrogenation catalyst. *Appl. Catal. A Gen.* **2019**, *575*, 93–100. [CrossRef]
8. Thanh, N.T.K.; Maclean, N.; Mahiddine, S. Mechanisms of Nucleation and Growth of Nanoparticles in Solution. *Chem. Rev.* **2014**, *114*, 7610–7630. [CrossRef] [PubMed]
9. Ng, C.K.; Karahan, H.E.; Loo, S.; Chen, Y.; Cao, B. Interfaces. Biofilm-Templated Heteroatom-Doped Carbon-Palladium Nanocomposite Catalyst for Hexavalent Chromium Reduction. *ACS Appl. Mater. Interfaces* **2019**, *11*, 24018–24026. [CrossRef] [PubMed]
10. Wu, X.; Zhao, F.; Rahunen, N.; Varcoe, J.R.; Avignone-Rossa, C.; Thumser, A.E.; Slade, R.C.T. A Role for Microbial Palladium Nanoparticles in Extracellular Electron Transfer. *Angew. Chem. Int. Ed.* **2011**, *50*, 427–430. [CrossRef] [PubMed]
11. Xu, H.; Tan, L.; Cui, H.; Xu, M.; Xiao, Y.; Wu, H.; Dong, H.; Liu, X.; Qiu, G.; Xie, J. Characterization of Pd(II) biosorption in aqueous solution by Shewanella oneidensis MR-1. *J. Mol. Liq.* **2018**, *255*, 333–340. [CrossRef]
12. Li, Q.; Zhang, S.; Xuan, W.; Zhou, H.; Tian, W.; Deng, X.; Huang, J.; Xie, Z.; Liu, F.; Liu, X.; et al. Microbial synthesis of highly dispersed nano-Pd electrocatalyst for oxygen reduction reaction. *Int. J. Hydrogen Energy* **2021**, *46*, 26886–26896. [CrossRef]
13. Courtney, J.; Deplanche, K.; Rees, N.V.; Macaskie, L.E. Biomanufacture of nano-Pd(0) by Escherichia coli and electro-chemical activity of bio-Pd(0) made at the expense of H-2 and formate as electron donors. *Biotechnol. Lett.* **2016**, *38*, 1903–1910. [CrossRef] [PubMed]
14. Yates, M.D.; Cusick, R.D.; Logan, B.E. Extracellular Palladium Nanoparticle Production using Geobacter sulfurreducens. *ACS Sustain. Chem. Eng.* **2013**, *1*, 1165–1171. [CrossRef]
15. Cui, J.; Zhu, N.; Kang, N.; Ha, C.; Shi, C.; Wu, P. Biorecovery mechanism of palladium as nanoparticles by Enterococcus faecalis: From biosorption to bioreduction. *Chem. Eng. J.* **2017**, *328*, 1051–1057. [CrossRef]
16. de Vargas, I.; Macaskie, L.E.; Guibal, E. Biosorption of palladium and platinum by sulfate-reducing bacteria. *J. Chem. Technol. Biotechnol.* **2004**, *79*, 49–56. [CrossRef]
17. Zhou, C.; Wang, Z.; Marcus, A.K.; Rittmann, B.E. Biofilm-enhanced continuous synthesis and stabilization of palladium nanoparticles (PdNPs). *Environ. Sci. Nano* **2016**, *3*, 1396–1404. [CrossRef]
18. Suja, E.; Nancharaiah, Y.V.; Venugopalan, V.P. Biogenic nanopalladium production by self-immobilized granular biomass: Application for contaminant remediation. *Water Res.* **2014**, *65*, 395–401. [CrossRef] [PubMed]

19. Su, J.; Deng, L.; Huang, L.; Guo, S.; Liu, F.; He, J. Catalytic oxidation of manganese(II) by multicopper oxidase CueO and characterization of the biogenic Mn oxide. *Water Res.* **2014**, *56*, 304–313. [CrossRef] [PubMed]
20. Saravanan, A.; Kumar, P.S.; Karishma, S.; Vo, D.-V.N.; Jeevanantham, S.; Yaashikaa, P.R.; George, C.S. A review on biosynthesis of metal nanoparticles and its environmental applications. *Chemosphere* **2021**, *264*, 128580. [CrossRef] [PubMed]
21. Xiong, L.; Chen, J.-J.; Huang, Y.-X.; Li, W.-W.; Xie, J.-F.; Yu, H.-Q. An oxygen reduction catalyst derived from a robust Pd-reducing bacterium. *Nano Energy* **2015**, *12*, 33–42. [CrossRef]
22. Liu, J.; Huang, Z.; Cai, K.; Zhang, H.; Lu, Z.; Li, T.; Zuo, Y.; Han, H. Clean Synthesis of an Economical 3D Nanochain Network of PdCu Alloy with Enhanced Electrocatalytic Performance towards Ethanol Oxidation. *Chem. Eur. J.* **2015**, *21*, 17779–17785. [CrossRef] [PubMed]
23. Chang, J.; Feng, L.; Liu, C.; Xing, W.; Hu, X. An Effective Pd-Ni2P/C Anode Catalyst for Direct Formic Acid Fuel Cells. *Angew. Chem. Int. Ed.* **2014**, *53*, 122–126. [CrossRef] [PubMed]
24. Tang, J.; Liu, J.; Li, C.; Li, Y.; Tade, M.O.; Dai, S.; Yamauchi, Y. Synthesis of Nitrogen-Doped Mesoporous Carbon Spheres with Extra-Large Pores through Assembly of Diblock Copolymer Micelles. *Angew. Chem. Int. Ed.* **2015**, *54*, 588–593. [CrossRef]
25. Yates, M.D.; Cusick, R.D.; Ivanov, I.; Logan, B.E. Exoelectrogenic Biofilm as a Template for Sustainable Formation of a Catalytic Mesoporous Structure. *Biotechnol. Bioeng.* **2014**, *111*, 2349–2354. [CrossRef]
26. Sun, D.; Zhang, G.; Jiang, X.; Huang, J.; Jing, X.; Zheng, Y.; He, J.; Li, Q. Biogenic flower-shaped Au-Pd nanoparticles: Synthesis, SERS detection and catalysis towards benzyl alcohol oxidation. *J. Mater. Chem. A* **2014**, *2*, 1767–1773. [CrossRef]
27. Kong, W.Q.; Lin, J.Y.; He, X.; Cheng, Y.Y.; Zhang, X.S.; Deng, G.Z.; Han, R.S.; Wu, C. Reduction pathway and mechanism of chloronitrobenzenes synergistically catalyzed by bioPd and Shewanella oneidensis MR-1 assisted by calculation. *Chemosphere* **2017**, *187*, 62–69. [CrossRef]
28. Song, X.; Shi, X. Biosynthesis of Ag/reduced graphene oxide nanocomposites using Shewanella oneidensis MR-1 and their antibacterial and catalytic applications. *Appl. Surf. Sci.* **2019**, *491*, 682–689. [CrossRef]
29. Zhang, S.; Li, Q.; Zhou, H.; Xuan, W.; Liang, Y.; Xie, Z.; Liu, F. Scalable preparation of Pd/bacteria-rGO(CNT, Ketjen) composites for efficient oxygen reduction catalyst. *Int. J. Hydrogen Energy* **2021**, *46*, 5664–5676. [CrossRef]
30. Fu, G.-T.; Jiang, X.; Wu, R.; Wei, S.-H.; Sun, D.-M.; Tang, Y.-W.; Lu, T.-H.; Chen, Y. Arginine-Assisted Synthesis and Catalytic Properties of Single-Crystalline Palladium Tetrapods. *ACS Appl. Mater. Interfaces* **2014**, *6*, 22790–22795. [CrossRef]
31. Rotaru, A.-E.; Jiang, W.; Finster, K.; Skrydstrup, T.; Meyer, R.L. Non-enzymatic palladium recovery on microbial and synthetic surfaces. *Biotechnol. Bioeng.* **2012**, *109*, 1889–1897. [CrossRef] [PubMed]
32. Ramalingam, B.; Parandhaman, T.; Das, S.K. Antibacterial Effects of Biosynthesized Silver Nanoparticles on Surface Ultrastructure and Nanomechanical Properties of Gram-Negative Bacteria viz *Escherichia coli Pseudomonas aeruginosa*. *ACS Appl. Mater. Interfaces* **2016**, *8*, 4963–4976. [CrossRef] [PubMed]
33. Zhou, C.; Ontiveros-Valencia, A.; Wang, Z.; Maldonado, J.; Zhao, H.-P.; Krajmalnik-Brown, R.; Rittmann, B.E. Palladium Recovery in a H-2-Based Membrane Biofilm Reactor: Formation of Pd(0) Nanoparticles through Enzymatic and Auto-catalytic Reductions. *Environ. Sci. Technol.* **2016**, *50*, 2546–2555. [CrossRef] [PubMed]
34. Martins, M.; Mourato, C.; Sanches, S.; Noronha, J.P.; Barreto Crespo, M.T.; Pereira, I.A.C. Biogenic platinum and palladium nanoparticles as new catalysts for the removal of pharmaceutical compounds. *Water Res.* **2017**, *108*, 160–168. [CrossRef] [PubMed]
35. Li, Y.; Dai, Y.; Yang, Z.; Li, T. Controllable synthesis of palladium nanoparticles and their catalytic abilities in Heck and Suzuki reactions. *Inorg. Chim. Acta* **2014**, *414*, 59–62. [CrossRef]
36. Xie, J.; Zhang, X.; Zhang, H.; Zhang, J.; Li, S.; Wang, R.; Pan, B.; Xie, Y. Intralayered Ostwald Ripening to Ultrathin Nanomesh Catalyst with Robust Oxygen-Evolving Performance. *Adv. Mater.* **2017**, *29*, 1604765. [CrossRef]
37. Hu, K.-J.; Plant, S.R.; Ellis, P.R.; Brown, C.M.; Bishop, P.T.; Palmer, R.E. Atomic Resolution Observation of a Size-Dependent Change in the Ripening Modes of Mass-Selected Au Nanoclusters Involved in CO Oxidation. *J. Am. Chem. Soc.* **2015**, *137*, 15161–15168. [CrossRef]
38. Wang, L.; Wang, L.; Meng, X.; Xiao, F.-S. New Strategies for the Preparation of Sinter-Resistant Metal-Nanoparticle-Based Catalysts. *Adv. Mater.* **2019**, *31*, 1901905. [CrossRef]
39. Yuan, W.; Zhang, D.; Ou, Y.; Fang, K.; Zhu, B.; Yang, H.; Hansen, T.W.; Wagner, J.B.; Zhang, Z.; Gao, Y.; et al. Direct In Situ TEM Visualization and Insight into the Facet-Dependent Sintering Behaviors of Gold on TiO_2. *Angew. Chem. Int. Ed.* **2018**, *57*, 16827–16831. [CrossRef]
40. Zhan, W.; He, Q.; Liu, X.; Guo, Y.; Wang, Y.; Wang, L.; Guo, Y.; Borisevich, A.Y.; Zhang, J.; Lu, G.; et al. A Sacrificial Coating Strategy Toward Enhancement of Metal-Support Interaction for Ultrastable Au Nanocatalysts. *J. Am. Chem. Soc.* **2016**, *138*, 16130–16139. [CrossRef]
41. Zhan, W.; Shu, Y.; Sheng, Y.; Zhu, H.; Guo, Y.; Wang, L.; Guo, Y.; Zhang, J.; Lu, G.; Dai, S. Surfactant-Assisted Stabilization of Au Colloids on Solids for Heterogeneous Catalysis. *Angew. Chem. Int. Ed.* **2017**, *56*, 4494–4498. [CrossRef]
42. Patnaik, S.G.; Vedarajan, R.; Matsumi, N. BIAN Based Electroactive Polymer with Defined Active Centers as Metal-Free Electrocatalysts for Oxygen Reduction Reaction (ORR) in Aqueous and Nonaqueous Media. *ACS Appl. Energy Mater.* **2018**, *1*, 1183–1190. [CrossRef]
43. Zhang, Y.; Reed, A.; Kim, D.Y. Nitrogen doped carbon nano-onions as efficient and robust electrocatalysts for oxygen reduction reactions. *Curr. Appl. Phys.* **2018**, *18*, 417–423. [CrossRef]

44. Fujiwara, K.; Okuyama, K.; Pratsinis, S.E. Metal-support interactions in catalysts for environmental remediation. *Environ. Sci. Nano* **2017**, *4*, 2076–2092. [CrossRef]
45. Kiyani, R.; Parnian, M.J.; Rowshanzamir, S. Investigation of the effect of carbonaceous supports on the activity and stability of supported palladium catalysts for methanol electro-oxidation reaction. *Int. J. Hydrogen Energy* **2017**, *42*, 23070–23084. [CrossRef]
46. Perini, L.; Durante, C.; Favaro, M.; Perazzolo, V.; Agnoli, S.; Schneider, O.; Granozzi, G.; Gennaro, A. Metal-Support Interaction in Platinum and Palladium Nanoparticles Loaded on Nitrogen-Doped Mesoporous Carbon for Oxygen Reduction Reaction. *ACS Appl. Mater. Interfaces* **2015**, *7*, 1170–1179. [CrossRef]
47. Leng, L.; Xu, S.; Liu, R.; Yu, T.; Zhuo, X.; Leng, S.; Xiong, Q.; Huang, H. Nitrogen containing functional groups of biochar: An overview. *Bioresour. Technol.* **2020**, *298*, 122286. [CrossRef]
48. Liu, C.; Liu, Y.; Liu, R.; Lalancette, R.; Szostak, R.; Szostak, M. Palladium-Catalyzed Suzuki-Miyaura Cross-Coupling of N-Mesylamides by N-C Cleavage: Electronic Effect of the Mesyl Group. *Org. Lett.* **2017**, *19*, 1434–1437. [CrossRef]
49. Zhao, X.; Liu, D.; Guo, H.; Liu, Y.; Zhang, W. C–N bond cleavage of allylic amines via hydrogen bond activation with alcohol solvents in Pd-catalyzed allylic alkylation of carbonyl compounds. *J. Am. Chem. Soc.* **2011**, *133*, 19354–19357. [CrossRef]
50. Dai, W.-C.; Wang, Z.-X. Palladium-catalyzed coupling of azoles with 1-aryltriazenes via C-H/C-N cleavage. *Org. Chem. Front.* **2017**, *4*, 1281–1288. [CrossRef]
51. Hao, W.; Geng, W.; Zhang, W.-X.; Xi, Z. Palladium- Catalyzed One- Pot Three- or Four- Component Coupling of Aryl Iodides, Alkynes, and Amines through C similar to N Bond Cleavage: Efficient Synthesis of Indole Derivatives. *Chem. Eur. J.* **2014**, *20*, 2605–2612. [CrossRef] [PubMed]
52. Mian, M.M.; Liu, G.; Zhou, H. Preparation of N-doped biochar from sewage sludge and melamine for peroxymonosulfate activation: N-functionality and catalytic mechanisms. *Sci. Total Environ.* **2020**, *744*, 140862. [CrossRef] [PubMed]
53. Hou, Y.-N.; Zhang, B.; Yun, H.; Yang, Z.-N.; Han, J.-L.; Zhou, J.; Wang, A.-J.; Cheng, H.-Y. Palladized cells as suspension catalyst and electrochemical catalyst for reductively degrading aromatics contaminants: Roles of Pd size and distribution. *Water Res.* **2017**, *125*, 288–297. [CrossRef] [PubMed]
54. Ojani, R.; Raoof, J.B.; Safshekan, S. Photoinduced deposition of palladium nanoparticles on TiO_2 nanotube electrode and investigation of its capability forformaldehyde oxidation. *Electrochim. Acta* **2014**, *138*, 468–475. [CrossRef]
55. Xu, G.-R.; Wang, B.; Zhu, J.-Y.; Liu, F.-Y.; Chen, Y.; Zeng, J.-H.; Jiang, J.-X.; Liu, Z.-H.; Tang, Y.-W.; Lee, J.-M. Morphological and Interfacial Control of Platinum Nanostructures for Electrocatalytic Oxygen Reduction. *ACS Catal.* **2016**, *6*, 5260–5267. [CrossRef]
56. Hassan, K.M.; Hathoot, A.A.; Maher, R.; Azzem, M.A. Electrocatalytic oxidation of ethanol at Pd, Pt, Pd/Pt and Pt/Pd nano particles supported on poly 1,8-diaminonaphthalene film in alkaline medium. *RSC Adv.* **2018**, *8*, 15417–15426. [CrossRef]